Numerical and experimental study of wheel-rail impact vibration and noise generated at an insulated rail joint

Yang, Zhen; Boogaard, Anthonie; Chen, Rong; Dollevoet, Rolf; Li, Zili

DOI
10.1016/j.ijimpeng.2017.11.008

Publication date
2018

Document Version
Accepted author manuscript

Published in
International Journal of Impact Engineering

Numerical and experimental study of wheel-rail impact vibration and noise generated at an insulated rail joint

Zhen Yang[1,2], Anthonie Boogaard[1], Rong Chen[2], Rolf Dollevoet[1], Zili Li[1]

1. Delft University of Technology, Section of Railway Engineering, Stevinweg 1, 2628 CN, Delft, the Netherlands

2. MOE Key Laboratory of High-Speed Railway Engineering, Southwest Jiaotong University, Chengdu, Sichuan, China

Abstract

As essential track components for rail connections and signal transmission and control, insulated rail joints (IRJs) have been widely used in traditional and high-speed railways. However, the IRJ is considered as one of the weakest parts of railway track structures due to the significant discontinuities in stiffness and geometry. When a train runs over an IRJ, a wheel-rail impact occurs and it increases with train speed. The impact consequently leads to vibration and noise and accelerates track deterioration in the vicinity of the IRJ. This paper establishes an explicit finite element wheel-IRJ dynamic interaction model to simulate high-frequency impact vibration and noise generated at a typical IRJ in the Dutch railway network, and validates the model against a comprehensive hammer test and a pass-by measurement. Good agreements between the simulation and measurements indicate that the proposed model can effectively reproduce high-frequency impact vibration and noise up to 10 kHz. This paper also connects the dominant frequencies of wheel-IRJ impact vibration and noise with the dynamic behaviour of the target IRJ, which may contribute to the mitigation of impact vibration and noise at IRJs as well as to train-borne detection of deterioration types of IRJs.

Keywords: insulated rail joint (IRJ); explicit FEM; hammer test; pass-by; impact vibration and noise

1 Introduction

As essential track components for rail connections and signal transmission and control, insulated rail joints (IRJs) have been widely used in both traditional and high-speed railways. The performance of IRJs directly influences railway transportation safety. However, due to the significant stiffness and geometric discontinuities, the IRJ is considered as one of the weakest parts of railway track structures. When a train runs over an IRJ, wheel-rail impact occurs. This impact consequently leads to vibration and noise and accelerates track deterioration in the vicinity of the IRJ.

Numerous modelling work has been carried out to simulate wheel-rail impacts generated by IRJs. Because impact problems are inherently non-linear, the simulation models are required to be solved in the time domain. Computationally efficient analytical models have been applied to calculate wheel-rail interactions when material complexity and detailed contact solutions are of less concern [1-4]. Considering a reduction of bending stiffness at a joint, Kerr et al. [1] simplified the joint of a track model as a gap and connected rails and fishplates with Winkler-type springs, whose stiffness was calibrated by a static load measurement. Mandal et al. [2] idealised the dipped rail joint with a sinusoidal profile to analyse the impact forces considering both track design and operational parameters. Wu and Thompson [3] treated the joint of their model as a pin between two semi-infinite Timoshenko beams and calculated the wheel-IRJ interaction by a relative displacement excitation model proposed by Grassie et al. [5]. Kitagawa et al. [4] modified Wu and Thompson's model by replacing the pin with a complex spring to represent the joint, whose vibratory behaviour level was validated against a field test. However, these analytical models fail to address the issues of the complex wheel-IRJ impact contact solutions and high-frequency impact dynamics over 5 kHz.

With the development of computer technology, the numerical finite element method (FEM) has increasingly been used to predict degradations of IRJs due to complex wheel-IRJ impact contact [6-12]. Owing to the capability of coping with non-linear material properties and arbitrary discontinuous contact geometries, finite element (FE) contact models can provide more accurate and detailed contact solutions. Nevertheless, many FE IRJ models tend to apply prescribed wheel loads as their excitations: either static [6-9] or pre-calculated by a simplified wheel-rail interaction model [10]; hence high-frequency dynamic effects caused by impact contact cannot be fully considered [11].

To take account of complex impact contact and high-frequency wheel/rail dynamic effects, this study simulates a wheel-rail impact at a typical IRJ in the Dutch railway network by an explicit FEM, which has been proven to be effective for solving impact contact problems [12-15] and high-frequency wheel/rail dynamics [16, 17]. Performing the integration in the time domain with an explicit central difference scheme, the explicit FEM manages to reproduce high-frequency dynamic effects by detailed modelling of the structure of wheel/track system and employing a small time step. Moreover, the calculations of high-frequency wheel/rail dynamic responses and contact forces can be automatically coupled, as the wheel/rail dynamic responses calculated in each time step rely on the contact forces obtained in the previous time step and in return affect the contact forces updated in the next time step.

This paper first establishes a three-dimensional (3D) FE wheel-IRJ interaction model to simulate impact vibration and noise excited by the target IRJ, and then validates the model against a comprehensive hammer test and a pass-by measurement. Compared to the explicit FE impact models proposed in the previous research [12-17], this model is more sophisticated in track dynamics and comprehensively validated. The condition of the target IRJ and wheel-IRJ interaction model are described in Section 2. In Section 3, the track sub-model with an IRJ is calibrated and its dynamic behaviour is validated against a hammer test; the dynamic behaviour of the wheel sub-model is validated by a measurement reported in the literature [18]. Section 4 reports a pass-by measurement to validate the high-frequency (up to 10 kHz) impact vibration and noise predicted by the FE impact model. The main conclusions are drawn in Section 5.

2 Finite element model

2.1 Condition of the target IRJ

A typical Dutch IRJ without visible damage was selected as the study target in the trunk line Amsterdam-Utrecht of the Dutch railway network. The IRJ locates on a straight track with a maximum one-directional train speed of 130 km/h. In the track, UIC54 rails with an inclination of 1/40 are supported by NS90 sleepers every 0.6 m except in the proximity of the IRJ, where a pair of adjacent timber sleepers with a distance of 0.24 m are employed to reduce the deflection of the joint and absorb vibration caused by wheel-IRJ impacts. Fig. 1 shows the in-situ condition of the target IRJ.

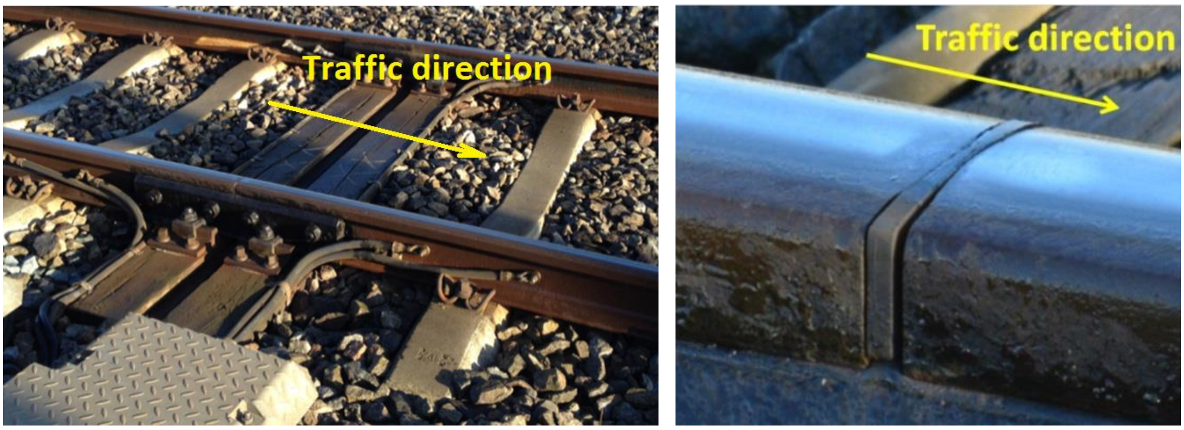

(a) General condition (b) Close-up of the end-post

Figure 1: In-situ condition of the target IRJ

2.2 Wheel-IRJ interaction model

A 3D FE wheel-IRJ dynamic interaction model, as shown in Fig. 2 (a), was established in this study. The model includes a 10-m length of half-track with an IRJ in the middle and a half-wheelset with the sprung mass of the car body and bogie. The wheel geometry corresponds to that of a passenger car wheel of the Dutch railway with the standard profile of S1002. The IRJ, composed of 2 fishplates, 4 pairs of bolts and a 6 mm gap, was modelled in detail with fine meshes (see close-up at upper left corner of Fig. 2 (b)). Since the value of elastic modulus of the end-post (insulation layer between two rail ends) is much lower than those of the rails and the presence of air gap (shown in Fig. 1 (b)) may result in free rail-end [19], the end-post layer was omitted in the model and simplified as a gap. Free boundaries were used on the rail ends at the joint, whereas non-reflecting boundaries were defined at the far ends of the rails. The wheel, rail and sleepers were modelled using 8-node solid elements. To achieve accurate solutions with a reasonable model size, non-uniform meshing was used and regular discretization was allocated at the wheel-rail contact area. The mesh size is 1 mm around the initial position of wheel-rail contact and within the 0.2-m length of solution zone (see close-up at upper left corner of Fig. 2 (b)). The car body and bogie were modelled as mass elements connected to the wheelset by the primary suspension of the vehicle with parallel linear springs and viscous dampers. The two neighbouring timber sleepers beneath the IRJ and the concrete sleepers modelled elsewhere were differentiated by their geometries and material properties. The baseplate fastening system used on the timber sleepers and the Vossloh fastening system on the concrete sleepers were modelled by crossed spring and damper elements (see close-up at lower right corner of Fig. 2 (b)), and adopted different linear stiffness and damping parameters (see table 1). The ballast was simplified as vertical spring and damper elements, with the displacements constrained in the lateral and longitudinal directions. Since the stiffness and damping parameters used to model the fastenings and ballast can hardly be measured directly in the field, these parameters were calibrated in this study by fitting the simulated frequency response functions (FRF) to the measurement results, which will be illustrated in detail in Section 3. Bi-linear elastoplastic material properties were applied to the wheel and rail models. The calibrated stiffness and damping parameters, as well as the nominal material properties applied in the model, are listed in table 1.

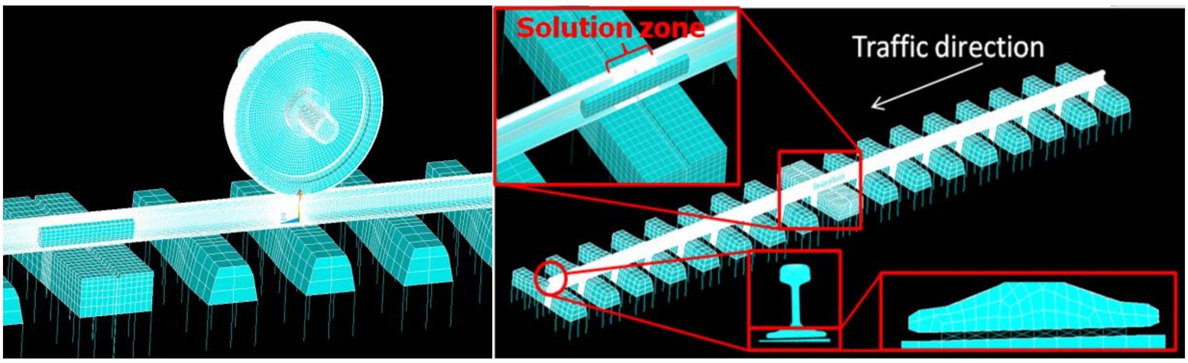

(a) Wheel-IRJ interaction model (b) Track model with IRJ (IRJ sub-model)

Figure 2: Finite element wheel-IRJ dynamic interaction model

Parameters		Nominal values	Parameters			Calibrated values
Rails and fishplates material	Young's modulus	210 GPa	Baseplate fastening	Vertical	Stiffness	86.7 MN/m
	Poisson's ratio	0.3			Damping	45000 Ns/m
	Density	7800 kg/m^3		Lateral	Stiffness	150 MN/m
	Yield stress	500 MPa			Damping	40000 Ns/m
	Tangent modulus	21 GPa	Vossloh fastening	Vertical	Stiffness	195 MN/m
Timber sleeper material	Young's modulus	20 GPa			Damping	67500 Ns/m
	Poisson's ratio	0.3		Lateral	Stiffness	100 MN/m
	Density	1300 kg/m^3			Damping	40000 Ns/m
Concrete sleeper material	Young's modulus	38.4 GPa	Ballast	Vertical	Stiffness	45 MN/m
	Poisson's ratio	0.2			Damping	32000 Ns/m
	Density	2520 kg/m^3	bolt pretension			12.5 kN

Table 1: The values of parameters used in the model

3 Calibration and validation of sub-models

In order to accurately predict wheel-IRJ impact interaction and the consequent vibration and noise, the dynamic behaviour of the track and wheel sub-models is validated in this section. The sub-model of the track with an IRJ, IRJ sub-model for short, was established corresponding to the target IRJ of Fig. 1. As shown in Fig. 2 (b), the IRJ sub-model excludes the wheel-sub model and car bodies presented in Fig. 2 (a).

The dynamic behaviour of track structures is generally characterised by frequency response functions (FRFs) due to the infinite structural nature [18]. Typical resonant frequencies of a track can be deduced according to its FRFs [20]. Hammer test is a widespread method for the identification of the FRFs of track structures [10, 21-23], but its application specifically to IRJs is limited. Recently, Oregui et al. [24] performed a systematic hammer measurement on IRJs to assess their health conditions, but their work only investigated dynamic behaviour of the IRJs in the vertical direction.

This study conducted a more comprehensive hammer test to measure the FRFs, in terms of accelerances, of the target IRJ not only in the vertical direction but in the lateral direction as well, since both of them are responsible for the noise radiation from the track. In this paper, the measured direct accelerances (response and excitation are measured in the same direction and location [25]) are used to calibrate the stiffness and damping parameters involved in the FE IRJ sub-model by fitting their levels and resonant frequencies to the simulation results, as described in [10, 23, 26, 27]; the measured transfer accelerances (response and excitation are measured in the same direction but different locations [25]), cross-accelerances (response and excitation are measured in different directions [25])) and decay rate of the track are then used to validate the dynamic behaviour of the calibrated track sub-model.

3.1 Set-up of the hammer test

Fig. 3 shows the set-up of the hammer test employed to identify the accelerances of the target IRJ. The FRFs of tracks without IRJs are normally measured at two track sections: on-support and mid-span [10, 20-24], where different responses are expected. This study added a third section around the rail-end just after the IRJ along the train travel direction, where a significant dynamic impact can be expected during a train pass-by. Six accelerometers (B&K 4514, denoted as 1-6 in Fig. 3) were placed at the three sections: three on the rail top and the other three on the field side of the rail head (see the close-up of Fig. 3), respectively, used to measure the vertical and lateral responses. Two accelerometers (IMI623C00, ensuring electric insulation between two rails in the measurement, denoted as 7 and 8 in Fig. 3) were placed on the rail top before the joint, respectively at the sections of rail-end and on-support, to detect vibration transmission to the other side of the joint.

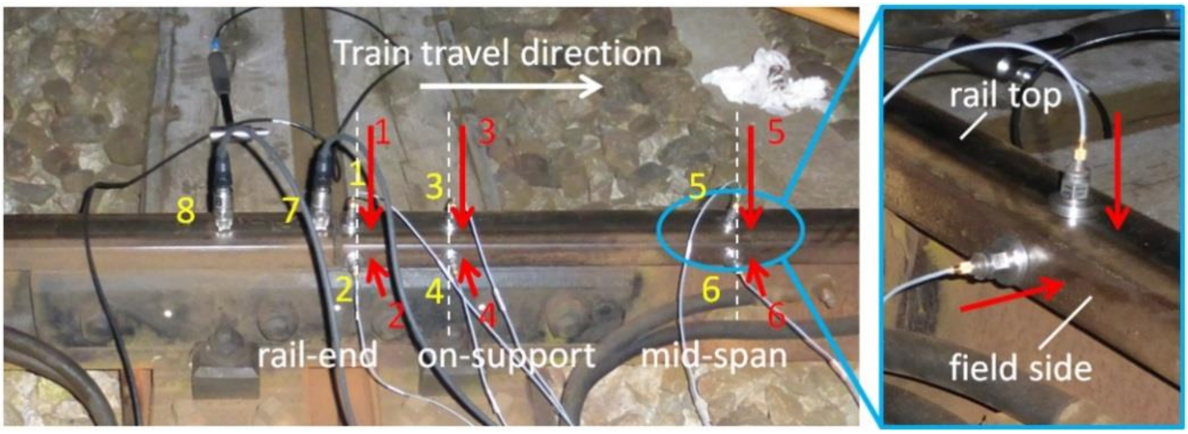

Figure 3: Distribution of accelerometers and force excitation points

(The yellow numbers 1-8 denote the accelerometers placed at the IRJ and the red arrows 1-6 indicate the positions and directions of the hammer excitations)

A hammer (PCB 086D05) with a hard metal tip (PCB 084B03) was used in the measurement to obtain high-frequency excitations. The hammer excitations were conducted as close as possible to the accelerometers 1-6, indicated by the red arrows 1-6 in Fig. 3. The excitation and response signals of 10 impacts were recorded at each hitting position. The spectra of the excitation loads at the six hitting positions, produced by averaging 10 impacts, are depicted in Fig. 4. The 3 dB drop (limit of very reliable range [23]) and 10 dB drop (limit of sufficiently reliable range [23]) occur at about 3.5 kHz and 5 kHz, respectively, indicating that the valid frequency range of the hammer-excited signals can reach up to 5 kHz.

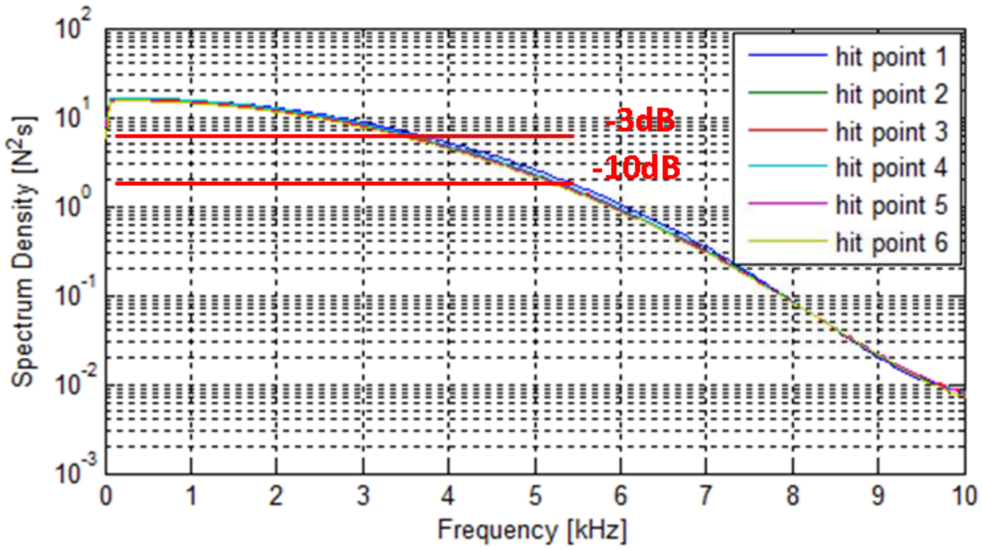

Figure 4: Valid frequency range determined by the spectra of excitation forces (within 3 dB drop: very reliable range; within 10 dB drop: reliable range [23])

The reliability of hammer test can be assessed by the coherence of the response signals excited by hammer impacts. Since the dynamic behaviour of the target IRJ under wheel-rail impacts is of particular interest in this study and wheel-rail impacts occur more or less at the rail-end section after the joint, the coherence of the response signals under the vertical hammer excitations at the position 1 (see Fig. 3) is presented here. The coherence curves of the response signals of the eight measurement points (denoted as 1-8 in Fig. 3) excited by the 10 hammer impacts at the position 1 are depicted in Fig. 5 (a) and (b). Excellent coherence over 0.9 in the whole frequency range of interest was obtained for the vertical responses (positions 1, 3, 5, 7, 8), whereas for the lateral responses (positions 2, 4, 6) lower coherence was observed at some frequency bands: around 360 Hz, 1160 Hz and over 3 kHz, probably due to that the cross-accelerance is more sensitive to the positions and directions of excitations and responses [22]. The good coherence of the lateral responses excited by the hammer in the lateral direction in Fig. 5 (c) indicates the testing signals in the lateral directions are also reliable.

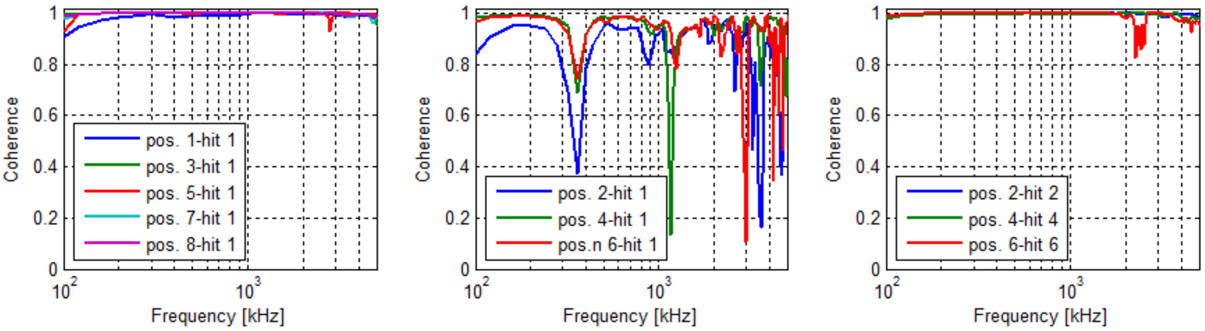

(a) vertical responses by the vertical excitation at 1 | (b) lateral responses by the vertical excitation at 1 | (c) lateral responses by lateral excitations

Figure 5: Coherence curves of the responses at the eight measurement points

3.2 IRJ sub-model calibration

As indicated by the coherence analysis, the direct accelerances and transfer accelerances were more reliably measured than the cross-accelerances. This study thus applied the measured direct accelerances as the reference to calibrate the stiffness and damping parameters involved in the FE IRJ sub-model. The accelerances of the IRJ sub-model were calculated by reproducing the hammer test with an explicit time integration method, as illustrated in [27]. The simulated excitations were applied in both the vertical and lateral directions at the three sections of the IRJ sub-model, respectively, as the measurement.

The closest fits of the simulated and measured vertical and lateral direct accelerances are depicted in Fig. 6 and 7, respectively. The measurement results shown here are the averages of the 10 times hammer-excited signals. Fig. 6 shows that the tendencies and resonant frequencies of the simulated vertical accelerances match the measurement. The measured typical track (anti-) resonances of the f_2 (rail mass on the fastening stiffness [22]), f_a (sleepers vibrate on the ballast and pad stiffness [22]), 1st and 2nd order vertical pinned-pinned of the target IRJ are 280 Hz, 440 Hz, 1050 Hz and 2750 Hz, respectively, whereas those from the simulation are 260 Hz, 460 Hz, 1100 Hz and 2550 Hz, respectively. The vertical accelerance of the rail-end section is similar to that of the on-support section between 200 and 600 Hz, in which frequency range a rail behaves like a mass and its dynamic behaviour is mainly dominated by supports [18]. Over 4 kHz, the response of the rail-end section is evidently higher than the other two sections, presenting a high-intensity dynamic feature. That is probably related to the reduction of the vertical structural stiffness at the joint, which is similar to the free end of a cantilever beam [4].

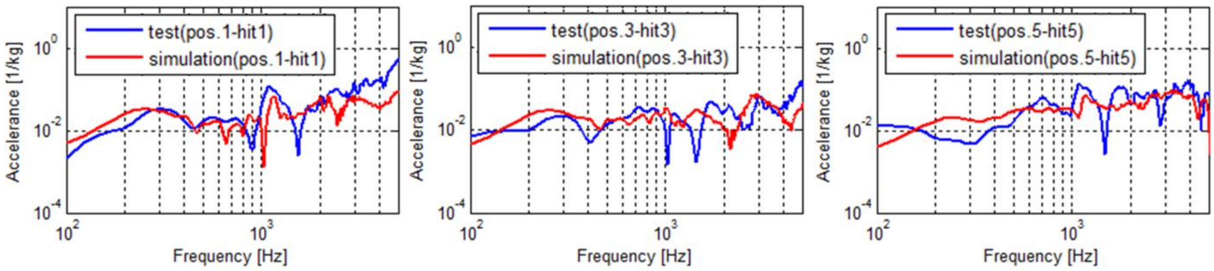

(a) Rail-end (position 1) (b) On-support (position 3) (c) Mid-span (position 5)

Figure 6: Fitting vertical accelerances (red line: simulation; blue line: test)

The general levels of the lateral direct accelerances shown in Fig. 7 are higher than the vertical ones shown in Fig 6. The tendencies and levels of the measured and simulated lateral direct accelerances are well fitted in Fig. 7. The lateral pinned-pinned resonance, less pronounced than the vertical one, occurs at about 550 Hz in the measurement and 600 Hz in the simulation. More oscillations can be observed in the simulation results between 600-1300 Hz, which could be influenced by the modelling of the fastening systems. Although an improved fastening model represented by crossed linear spring and damper elements managed to take into account the lateral dynamics, it failed to fully reproduce the modes of real fastenings comprised of rail pads and clamps [26]. The deviation at the low frequency below

200 Hz is probably related to the simplification of the ballast model, whose displacements were constrained in the lateral and longitudinal directions.

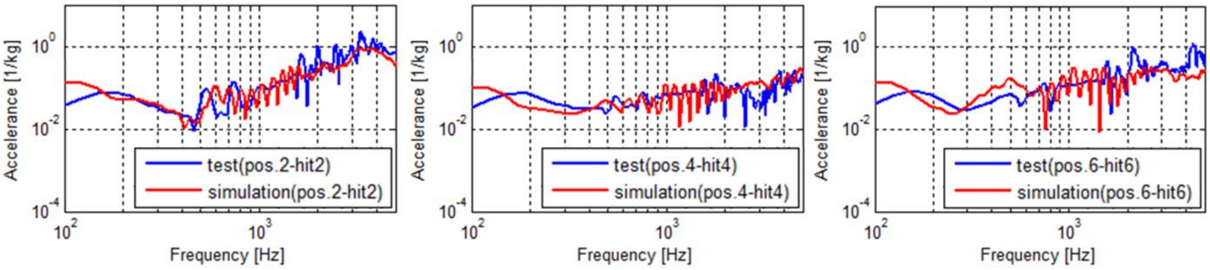

(a) Rail-end (position 2) (b) On-support (position 4) (c) Mid-span (position 6)

Figure 7: Fitting lateral accelerances (red line: simulation; blue line: test)

It can be concluded from the analysis of the direct accelerances that the dynamic behaviour of the rail-end section has a high-intensity feature due to the reduction of bending stiffness. The stiffness and damping parameters calibrated by the direct accelerances are then adopted in the simulations of the transfer accelerances and cross-accelerances, track decay rate and wheel-rail impact at the target IRJ.

3.3 Validation of transfer and cross-accelerances

The vibration responses of the IRJ under the vertical hammer excitation at the rail-end section (position 1 in Fig. 3) are studied for the IRJ sub-model validation. The transfer and cross-accelerances, including phases, simulated by the calibrated IRJ sub-model are compared with the measurement in Fig. 8. Good agreements for the transfer accelerances and reasonable agreements for the cross-accelerances are achieved. It is believed that the deviations of the cross-accelerances at 120 Hz and 500-1300 Hz are respectively caused by the simplification of the ballast model and the linear spring/damper representations of the rail pads models, as analysed in the lateral direct accelerances.

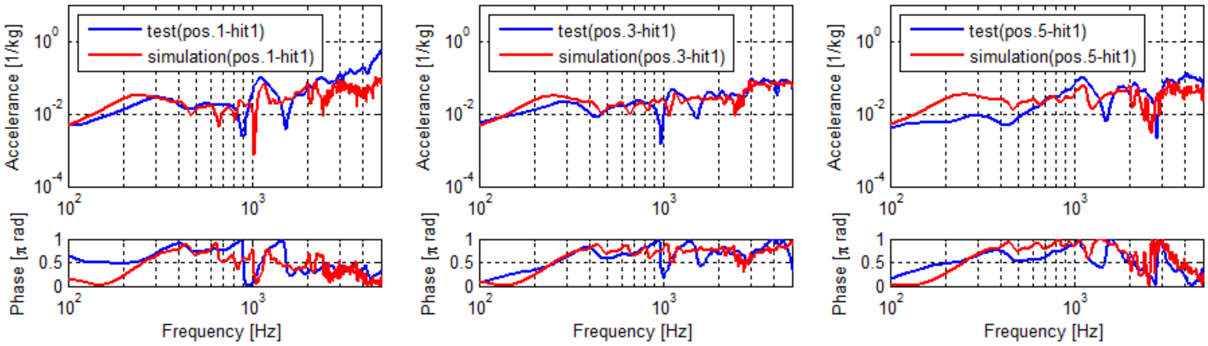

(a) Rail-end (position 1) (b) On-support (position 3) (c) Mid-span (position 5)

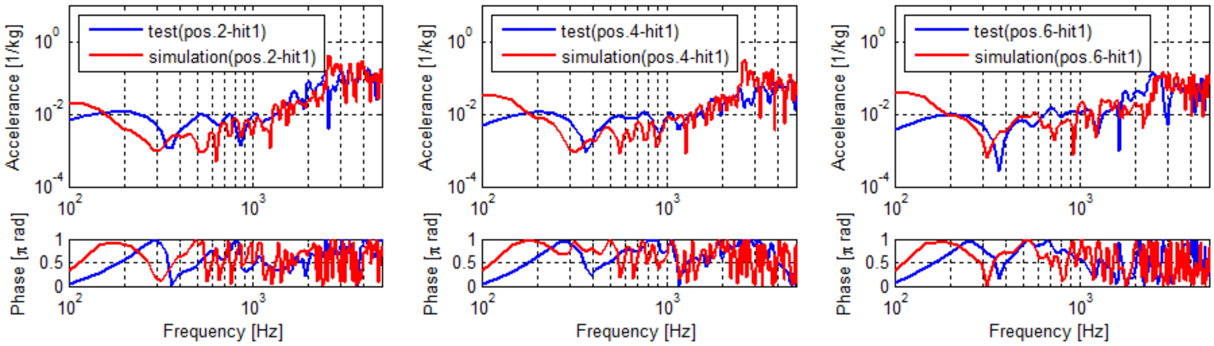

(d) Rail-end (position 2) (e) On-support (position 4) (f) Mid-span (position 6)

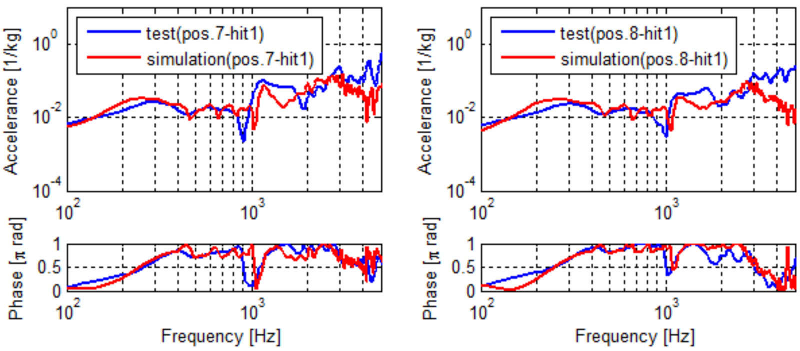

(g) Rail-end (position 7) (h) On-support (position 8)

Figure 8: Validations of transfer and cross-accelerances (red line: simulation; blue line: test. transfer accelerances: (a)-(c) and (g)-(h); cross-accelerances: (d)-(f))

3.4 Validation of decay rate

The validation of track decay rate is also important for the accurate prediction of pass-by vibration and noise [28]. Owing to the reciprocity, the decay rate of a track with periodical structural characteristics is normally measured by a roving hammer method for operational convenience [29]. The comparison of the transfer accelerances measured at the on-support (position 3) and mid-span (position 5) sections shown in Fig. 9 (a) indicates the reciprocity can be basically obeyed there, whereas Fig. 9 (b) and (c) show that the reciprocity can hardly be satisfied at the rail-end section in the high-frequency range over 3 kHz. Therefore, this study employed a roving sensor approach to measuring the decay rate of the target IRJ. The hammer excitations were exerted at the rail-end section after the joint (position 1 in Fig. 3), where wheel-IRJ impacts are expected to occur; Nine accelerometers (B&K 4514, denoted as 1-9 in Fig. 10) were employed in the measurement and a 5-meter section of the track (8 sleeper spans) just after the IRJ could be covered by roving the sensors once. Referring to the hammer excitation positions suggested in the roving hammer test of decay rate [29], the sensor distribution schemes adopted in this study are shown in Fig. 10 (a), and the corresponding in-situ conditions are shown in Fig. 10 (b) and (c).

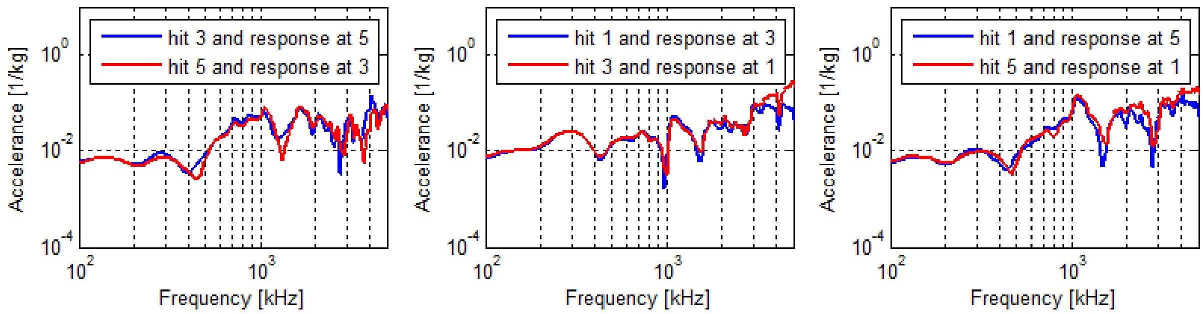

(a) Position 3 & 5 (b) position 1 & 3 (c) position 1 & 5

Figure 9: Comparisons of measured transfer accelerances

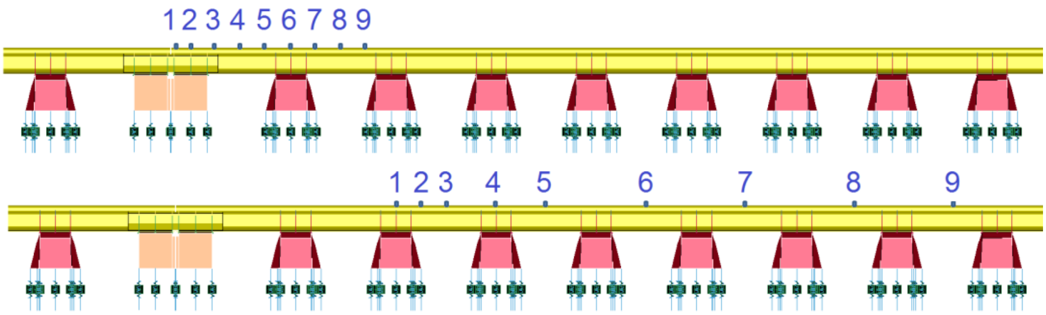

(a) Sketch of sensor distributions before (upper graph) and after (lower graph) roving

(b) Sensor distribution before roving (c) Sensor distribution after roving

Figure 10: Sensor distribution schemes in the decay rate test

The hammer test of the decay rate was also reproduced by the proposed FE IRJ sub-model with an explicit time integration method. Fig. 11 compares the time histories of the simulated vibration of the 18 response positions (9 sensors × 2 rounds) with those obtained by the measurements. The measurement results shown here are also the averages of the 10 times excitations, as the accelerances analysed above. Good agreements can be observed in the vast majority of the comparisons. The simulated and measured vertical decay rates of the target IRJ are calculated based on these vibration responses [30] and compared in Fig. 12. Good agreements in terms of the peak, trough and average level in the comparison of the decay rate again validate the dynamic behaviour of the presented FE IRJ sub-model. The decay rate peaks at about 3 kHz and troughs at about 900 Hz and 4 kHz.

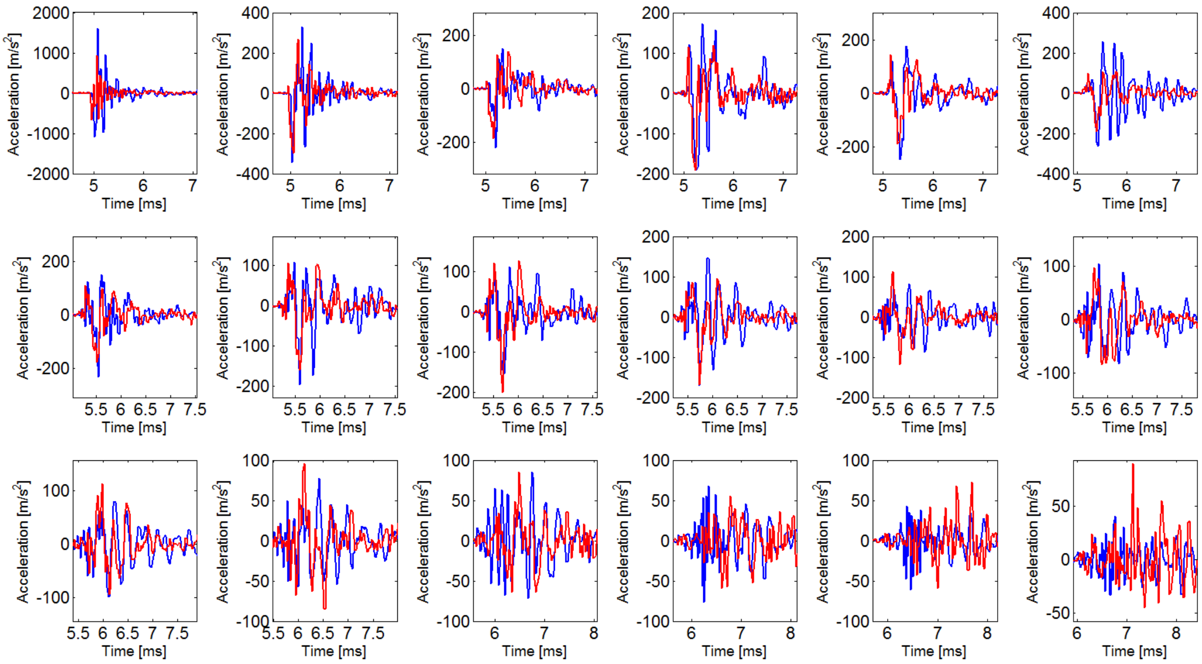

Figure 11: Comparison of acceleration responses (red line: simulation; blue line: test)

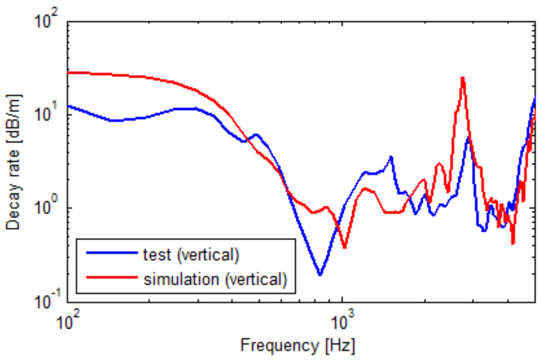

Figure 12: Validation of decay rate (red line: simulation; blue line: test)

3.5 Validation of the wheel sub-model

Although the dynamic behaviour of wheels may also be characterised with FRFs [31], this study characterised the dynamic behaviour of the FE wheel sub-mode with the modes and the corresponding natural frequencies and validated them against a measurement reported in [18], because the material damping of a wheel is generally very low and the exact value of the wheel modal damping is not critical for rolling noise prediction [18]. The frequency range of interest is 10 kHz in this study. All modes of the wheel sub-model within the frequency range of interest were identified by a modal analysis. For this, the same half-wheelset model as the explicit FE model shown in Fig. 2 (a) was used with the inner edge of its hub clamped. The calculated wheel modes under such a boundary condition can adequately represent the wheel dynamics under contact with the rail [32]. The identified natural frequencies of the axial and radial wheel modes are plotted in Fig. 13. Good agreement is observed when comparing the calculated results with the experimental wheel natural frequencies from [18], in which an NS-intercity wheel is measured for up to 5 kHz. All of these physical modes can be naturally included in the transient dynamic simulation when using the full FE model and a small time step [33].

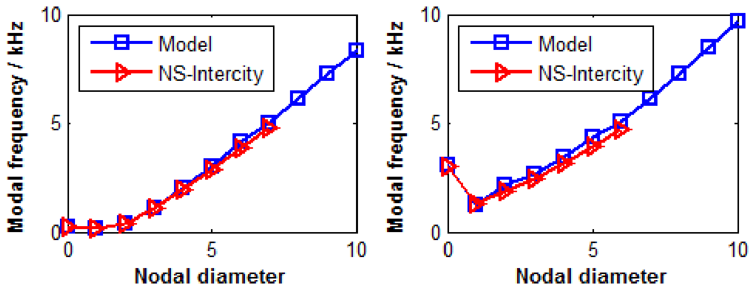

(a) Zero-nodal circles (b) Radial

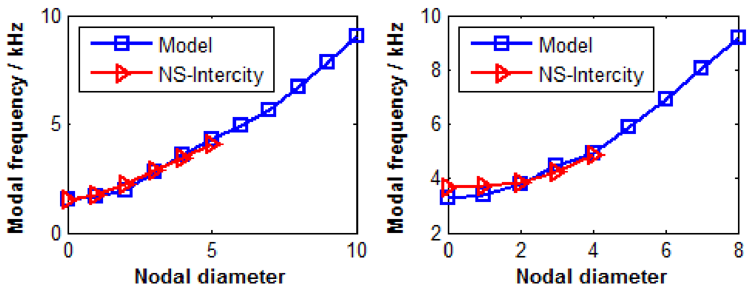

(c) One-nodal circles (d) Two-nodal circles

Figure 13 Wheel modes calculated by a finite element modal analysis (blue) compared with the measured results (red, from [18])

4 Impact vibration and noise during pass-by

The validations of the IRJ and wheel sub-models enable the FE dynamic interaction model for a transient impact simulation. The simulated impact vibration and noise are compared to the measurement results from a pass-by measurement in this section.

4.1 Set-up of the pass-by measurement

A pass-by measurement with a travelling speed of about 100 km/h was performed on the target IRJ on 19th February 2015. The vertical and lateral impact vibration, collected on the rail foot just after the joint (see Fig. 14 (a)), were measured by accelerometers PCB 352A60 (measurement range: ± 4950 m/s^2; frequency range (± 3 dB): 5 Hz-60 kHz) and B&K 4514 (measurement range: ± 980 m/s^2; frequency range (± 6 dB): 5 Hz-10 kHz), respectively. Two microphones B&K 4958 (measurement range: 28 -140 dB; frequency range (±1 dB): 28 Hz-20 kHz) were placed 1.5 m after the joint in the train running direction, and respectively 2.5 cm (Fig. 14 (b)) and 7.5 m (Fig. 14 (c)) away from the rail to record the near-field and far-field impact noise.

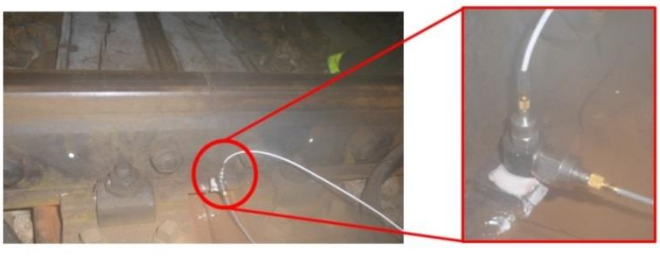

(a) Accelerometers used to measure impact vibration

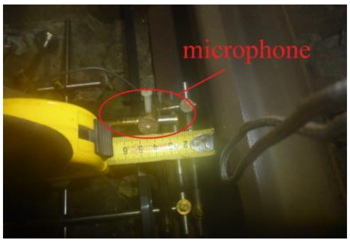

(b) Near-field microphone (c) Far-field microphone

Figure 14: Set-up of sensors in the pass-by measurement

4.2 Impact vibration

The pass-by measurement conducted at the target IRJ was reproduced by the 3D FE wheel-IRJ dynamic interaction model shown in Fig. 2(a) with an explicit time integration. A tiny time step (49 ns) was employed to meet Courant stability condition [34]. This, together with the fine meshing scheme applied in the model, guaranteed that high-frequency dynamic effects up to 10 kHz or higher can be reproduced. The transient dynamic simulation first employed a dynamic relaxation to make the wheel-track system reach an equilibrium state under gravity. The initial position of the wheel model is 1.32 m away from the joint, as shown in Fig. 2. A forward translation velocity and a corresponding rotational velocity were defined as initial conditions applied to all the nodes of the wheel model. The forward translation velocity, which is also the rolling velocity of the wheel, initially equalled to the wheel circumferential velocity, i.e. the product of the rotational velocity and the wheel radius. A driving torque was subsequently applied to the wheel axle as a load boundary condition, due to which the wheel rotational velocity increased so that the wheel circumferential velocity exceeded the rolling velocity. Consequently, creepage and traction force were generated between the wheel and rail when the wheel rolled along the rail from the initial position towards the joint. As the measurement, the simulated pass-by speed was 100 km/h and the impact vibration responses were calculated at the rail foot just after the joint in the model. The measured geometry of the target IRJ (Fig. 1 (b)) by a HandySCAN 3D laser scanner was applied to the FE model. Fig. 15 (a) and (b) show the rail top surface in the proximity to the joint model before and after applying the measured geometry, respectively. The measured geometric irregularities at 100-150 mm in the longitudinal direction, closer to the joint, is significantly larger than those elsewhere in Fig. 15 (b). We applied the measured geometry only to the vicinity of the joint rather than to the whole modelled rail surface, because the impact vibration and noise studied in this paper occurs transiently just when the wheel rolls over and hits the joint.

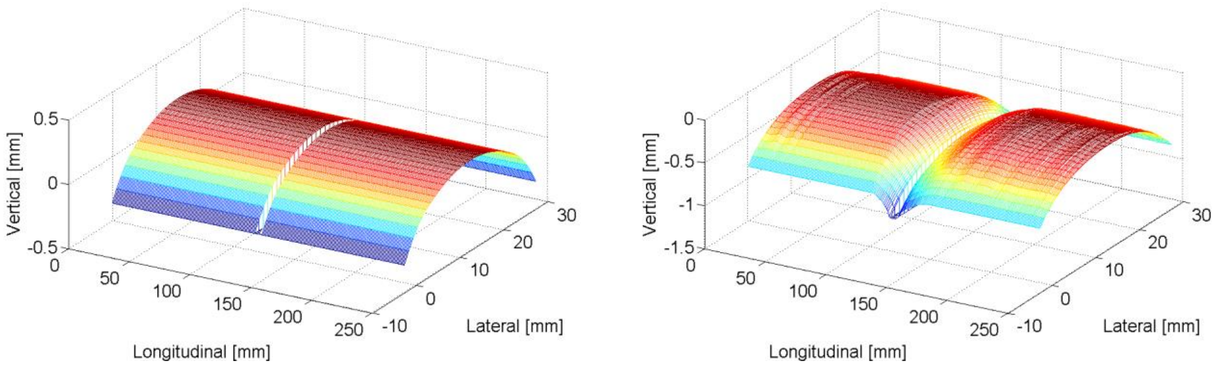

(a) Nominal geometry at an IRJ (b) Measured geometry at the target IRJ

Figure 15: Applying the realistic geometry to the IRJ (size of irregularity exaggerated)

The wheel/rail dynamic responses were obtained by averaging the motions of the elements attached to the wheel/rail volumes, while the contact forces were calculated by adding up the nodal forces within the wheel-rail contact patch. The wheel/rail dynamic responses calculated in each time step relied on the contact forces obtained in the previous time step, and in return affected the contact forces updated in the next time step; therefore, the full coupled solutions of wheel-rail dynamics and contact were obtained with a single simulation. The effects of transient wheel rotation were also included inherently.

Wavelet power spectrum (WPS) is considered appropriate for the investigation of non-stationary signals with local changes in the frequency components [17]. The WPSs of the simulated and measured impact vibration up to 10 kHz are compared on the same scale in Fig.

16. The results of the four pass-bys shown in Fig. 16 were successively measured when the four wheelsets of a coach passed the target IRJ. It can be seen that the simulated impact vibration agrees well with the pass-by measurement results in both the time domain and frequency domain. The good agreement of the impact vibration is based on the results of the sub-models validation and also demonstrates the accuracy of them. Both the measurement and simulation indicate that energy of the vertical impact vibration (upper row in Fig. 16) mainly concentrate on around 300 Hz and 1 kHz, corresponding to the f_2 and 1^{st} order pinned-pinned resonance, respectively. Typical impact vibration feature is shown by the WPSs of the vertical rail vibration: a prominent high-frequency energy concentration with a broadband from 4 kHz to 10 kHz or higher occurs transiently just at the wheel-IRJ impact. The WPSs of the lateral impact vibration (lower row in Fig. 16) imply that the dominant frequencies of the simulated lateral impact vibration range from 600-1200 Hz, slightly higher than the measurement results of 550-1000 Hz. These dominant frequency ranges may be associated with the lateral pinned-pinned resonance, as the simulated and measured lateral pinned-pinned resonances occur at approximate 600 Hz and 550 Hz, respectively, in line with the lower boundaries of the dominant frequency ranges of the lateral impact vibration. High-frequency components in the lateral impact vibration are much less pronounced than the vertical ones and vary to some extent in frequency range. This variation can be attributed to the randomness of the traffic, such as differences in wheel (worn) profile, suspension condition, hunting motion etc.

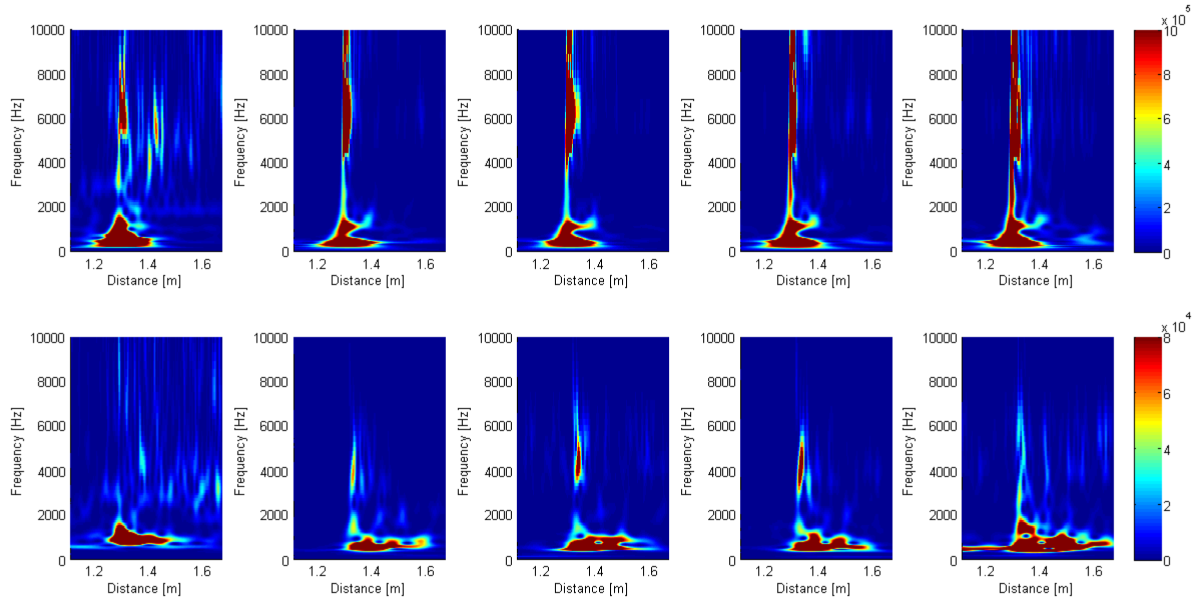

(a) Simulation (b) 1st pass-by (c) 2nd pass-by (d) 3rd pass-by (e) 4th pass-by

Figure 16: WPSs of the simulated and measured pass-by impact vibration (upper row: vertical impact vibration; lower row: lateral impact vibration. The unit of the colour bar is m/s^2)

4.3 Impact noise

The near-field and far-field impact noise were calculated by an efficient frequency-domain Rayleigh method [35] on the basis of the vibration velocities of the surface nodes of the wheel and rail pre-calculated in the explicit time integration. The collection positions of the near-field and far-field noise in the simulation corresponded to those in the measurement. A 100 Hz high-pass filter was applied to the noise signals to eliminate the influence of wind noise introduced by train pass-bys. The one-third octaves of the simulated and measured impact noise compared in Fig. 17 indicate that the predictions of the near-field and far-field impact noise are in good and reasonable agreements with the measurements in the frequency range of interest, respectively with deviations of less than 5 dB and 15 dB. The underestimation of both the near-field and far-field impact noise at around 500-600 Hz can be related to the deviations between the simulated and measured lateral track dynamics and impact vibration.

The omission of noise radiated by sleepers in the simulation may to some extent have contributed to the underestimation of the far-field noise at 400-500 Hz. The underestimation of the near-field noise around 800 Hz and 4 kHz may correspond to the two troughs of the decay rates at these frequencies in Fig. 12, which probably stem from the use of the track model with a length of 10 m: the noise contribution by the rail beyond the 10-m model cannot be included, resulting in the underestimation of the simulated noise especially when the decay rates are low. The overestimation of the far-field noise in the high-frequency range over 4 kHz might be caused by the limitation of the Rayleigh method, which assumes a radiating structure as a plane surface and is considered more accurate for near-field acoustic predictions [35]. A 30 dB noise reduction is observed from the near-field collection point just beside the rail web to the far-field one 7.5 meters away.

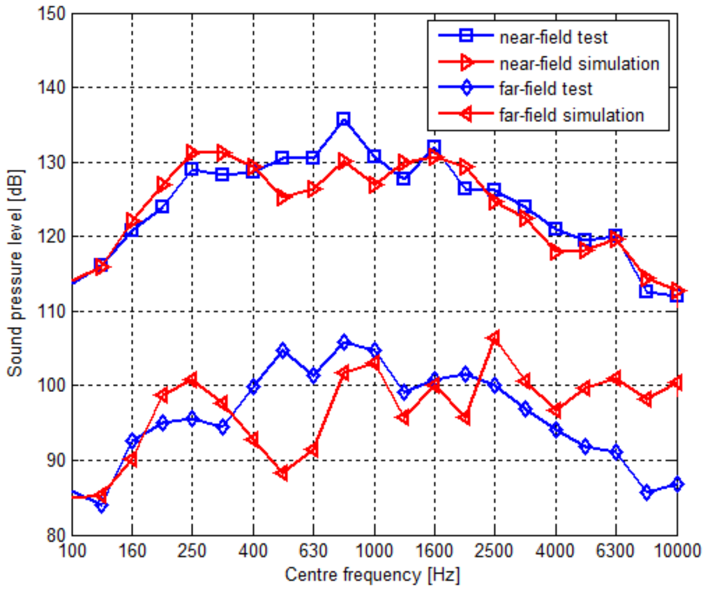

Figure 17: Comparisons of one-third octaves of impact noise

By comparing the impact vibration (Fig. 16) and noise (Fig. 17) to the dynamic behaviour (Fig. 6-7) of the target IRJ, we may deduce that high-frequency contents play more important roles in the impact vibration than impact noise. In addition, the f_2 resonance seems to contribute to the dominant frequency of the vertical impact vibration at about 300 Hz and the peak of the impact noise at 250 Hz, whereas the 1st order pinned-pinned resonance may determine the dominant frequency of the impact vibration at about 1 kHz and the 800 Hz peak of the impact noise. Furthermore, although the energy of the vertical impact vibration at the dominant frequency of 1 kHz is less pronounced and less long-lasting than that at 300 Hz, the 800 Hz peaks of the impact noise are higher than the 250 Hz ones (except the near-field simulation case). That is probably due to the contribution of the lateral impact vibration with a dominant frequency of 600-1000 Hz to the noise generation, as well as the low decay rate of the IRJ at about 900 Hz (troughs in Fig. 12).

5 Conclusion and future work

This paper presented a 3D transient explicit FE wheel-IRJ interaction model and validated the model by a comprehensive hammer test and pass-by measurement. The model is able to take into account complex wheel-rail dynamic interaction with non-linear material properties and arbitrary contact geometries; it should thus be able to calculate wheel-IRJ impact forces, vibration and noise directly and more accurately from the wheel-rail contact point of view, especially in the high-frequency range. The model also provides a possibility to analyse wheel/rail vibration in the vertical and lateral directions simultaneously.

By applying the in-situ measured geometries of the railhead to the IRJ model, the simulated impact vibration in both the time domain and the frequency domain agreed well with the pass-by measurement results, and the simulated impact noise was in reasonable agreement with the measurements, indicating that the explicit FEM is capable of reproducing impact vibration and noise excited by an IRJ up to 10 kHz.

The hammer test reveals that typical track resonances of the f_2 and f_a as well as the 1^{st} and 2^{nd} order vertical pinned-pinned of the target IRJ are around 280 Hz, 450 Hz, 1 kHz and 2.8 kHz, respectively; the rail-end section in the vicinity of the joint presents a high-intensity dynamic feature and reciprocity cannot be satisfied there in the high-frequency range over 3kHz; the decay rate of the target IRJ peaks at about 3 kHz and troughs at about 900 Hz and 4 kHz.

The dynamic behaviour of the target IRJ was not only used to validate the model but also connected with the dominant frequencies of the wheel-IRJ impact vibration and noise: the f_2 resonance and the 1^{st} order pinned-pinned resonance contribute significantly to the dominant frequencies of the impact vibration and noise; the vertical and lateral impact vibration with respective dominant frequencies of 1 kHz and 600-1000 Hz as well as the low decay rate of the target IRJ at about 900 Hz result in that the 1/3 octave spectrum of the impact noise peaks at around 800 Hz. These results indicate that the impact vibration and noise may be mitigated by controlling or re-designing the dynamic behaviour of IRJs: e.g. by damping the f_2 and 1^{st} pinned-pinned resonances or by a new design of the IRJ or support structures. The influence of dynamic behaviour of IRJs on impact vibration and noise deserves further investigations, and may contribute to the mitigation of impact vibration and noise generated by IRJs, as well as to train-borne detection of deterioration types of IRJs.

The main restriction of the presented model is the representation of the fastenings and ballast by the linear spring and viscous damper elements. When calibrating the stiffness and damping parameters, efforts were mainly taken to achieve the closest fit of the vertical accelerances because the vertical dynamics play more significant roles in the wheel-IRJ impact. The deviations of the lateral dynamics consequently affect the accuracies of the predictions of the lateral impact vibration and noise to some extent. The oscillations of the simulated lateral accelerances between 600-1300 Hz deserves a careful investigation in the future. A full FE representation of rail-pads with proper material parameters proposed in [26] could be an option to be employed to improve the accuracy of the lateral dynamics simulation. In addition, the effects of the track model length need to be further examined and the noise radiated by sleepers should be included in the future to improve the accuracies of the acoustic predictions. More train pass-bys may be measured to validate the model in a statistical way.

Acknowledgements

This work was supported by the China Scholarship Council; the Dutch railway infrastructure manager ProRail; and the open research fund of MOE Key Laboratory of High-speed Railway Engineering, Southwest Jiaotong University.

References

[1] A.D. Kerr, J.E. Cox, Analysis and tests of bonded insulated rail joints subjected to vertical wheel loads, Int J Mech Sci, 41 (1999) 1253-1272.
[2] N.K. Mandal, M. Dhanasekar, Y.Q. Sun, Impact forces at dipped rail joints, P I Mech Eng F-J Rai, 230 (2016) 271-282.
[3] T.X. Wu, D.J. Thompson, On the impact noise generation due to a wheel passing over rail joints, Journal of Sound and Vibration, 267 (2003) 485-496.
[4] T. Kitagawa, K. Murata, T. Kawaguchi, S. Tanaka, K. Nagakura, Experimental and Theoretical Studies on Impact Noise Generation due to Rail Joints, Notes Numer Fluid Me, 126 (2015) 55-62.
[5] S.L. Grassie, R.W. Gregory, D. Harrison, K.L. Johnson, The Dynamic-Response of Railway Track to High-Frequency Vertical Excitation, J Mech Eng Sci, 24 (1982) 77-90.
[6] Y.C. Chen, L.W. Chen, Effects of insulated rail joint on the wheel/rail contact stresses under the condition of partial slip, Wear, 260 (2006) 1267-1273.
[7] N.K. Mandal, M. Dhanasekar, Sub-modelling for the ratchetting failure of insulated rail joints, International Journal of Mechanical Sciences, 75 (2013) 110-122.
[8] J. Sandstrom, A. Ekberg, Numerical study of the mechanical deterioration of insulated rail joints, P I Mech Eng F-J Rai, 223 (2009) 265-273.
[9] A.K. Himebaugh, R.H. Plaut, D.A. Dillard, Finite element analysis of bonded insulated rail joints, Int J Adhes Adhes, 28 (2008) 142-150.
[10] E. Kabo, J.C.O. Nielsen, A. Ekberg, Prediction of dynamic train-track interaction and subsequent material deterioration in the presence of insulated rail joints, Vehicle System Dynamics, 44 (2006) 718-729.

[11] Z. Yang, Z.L. Li, R. Dollevoet, Modelling of non-steady-state transition from single-point to two-point rolling contact, Tribol Int, 101 (2016) 152-163.
[12] Z.F. Wen, X.S. Jin, W.H. Zhang, Contact-impact stress analysis of rail joint region using the dynamic finite element method, Wear, 258 (2005) 1301-1309.
[13] M. Pletz, W. Daves, H. Ossberger, A wheel set/crossing model regarding impact, sliding and deformation-Explicit finite element approach, Wear, 294 (2012) 446-456.
[14] W. Cai, Z.F. Wen, X.S. Jin, W.M. Zhai, Dynamic stress analysis of rail joint with height difference defect using finite element method, Eng Fail Anal, 14 (2007) 1488-1499.
[15] Z.L. Li, X. Zhao, R. Dollevoet, M. Molodova, Differential wear and plastic deformation as causes of squat at track local stiffness change combined with other track short defects, Vehicle Syst Dyn, 46 (2008) 237-246.
[16] Z. Yang, Z. Li, R.P.B.J. Dollevoet, An Explicit Integration Finite Element Method for Impact Noise Generation at a Squat, Notes Numer Fluid Me, 126 (2015) 63-70.
[17] M. Molodova, Z.L. Li, A. Nunez, R. Dollevoet, Validation of a finite element model for axle box acceleration at squats in the high frequency range, Comput Struct, 141 (2014) 84-93.
[18] D.J. Thompson, Railway Noise and Vibration : Mechanisms, Modelling and Means of Control, Elsevier, 2009.
[19] N. Zong, M. Dhanasekar, Experimental studies on the performance of rail joints with modified wheel/railhead contact, P I Mech Eng F-J Rai, 228 (2014) 857-877.
[20] D.J. Thompson, N. Vincent, Track Dynamic Behaviour at High Frequencies. Part 1: Theoretical Models and Laboratory Measurements, Vehicle System Dynamics, 24 (1995) 86-99.
[21] M. Oregui, Z. Li, R. Dollevoet, Identification of characteristic frequencies of damaged railway tracks using field hammer test measurements, Mech Syst Signal Pr, 54-55 (2015) 224-242.
[22] N. Vincent, D.J. Thompson, Track Dynamic Behaviour at High Frequencies. Part 2: Experimental Results and Comparisons with Theory, Vehicle System Dynamics, 24 (1995) 100-114.
[23] A.P. De Man, Dynatrack: A survey of dynamic railway track properties and their quality, in, TU Delft, 2002.
[24] M. Oregui, M. Molodova, A. Nunez, R. Dollevoet, Z. Li, Experimental Investigation Into the Condition of Insulated Rail Joints by Impact Excitation, Exp Mech, 55 (2015) 1597-1612.
[25] N. Maia, J. Silva, Theoretical and Experimental Modal Analysis, Research Studies Press LTD, England, 1998.
[26] M. Oregui, Z. Li, R. Dollevoet, An investigation into the modeling of railway fastening, Int J Mech Sci, 92 (2015) 1-11.
[27] M. Oregui, Z.L. Li, R. Dollevoet, An investigation into the vertical dynamics of tracks with monoblock sleepers with a 3D finite-element model, P I Mech Eng F-J Rai, 230 (2016) 891-908.
[28] J.N. Yang, D.J. Thompson, Time-domain prediction of impact noise from wheel flats based on measured profiles, Journal of Sound and Vibration, 333 (2014) 3981-3995.
[29] Railway applications - Noise emission - Characterisation of the dynamic properties of track sections for pass by noise measurements, in: EN 15461:2008+A1:2010(E), 2010.
[30] C.J.C. Jones, D.J. Thompson, R.J. Diehl, The use of decay rates to analyse the performance of railway track in rolling noise generation, Journal of Sound and Vibration, 293 (2006) 485-495.
[31] T.X. Wu, D.J. Thompson, A Hybrid Model for the Noise Generation Due to Railway Wheel Flats, Journal of Sound and Vibration, 251 (2002) 115-139.
[32] C. Glocker, E. Cataldi-Spinola, R.I. Leine, Curve squealing of trains: Measurement, modelling and simulation, Journal of Sound and Vibration, 324 (2009) 365-386.
[33] X. Zhao, Z.L. Li, The solution of frictional wheel-rail rolling contact with a 3D transient finite element model: Validation and error analysis, Wear, 271 (2011) 444-452.
[34] R. Courant, K. Friedrichs, H. Lewy, On the Partial Difference Equations of Mathematical Physics, IBM Journal of Research and Development, 11 (1967) 215-234.
[35] M. Amdi, M. Souli, J. Hargreaves, F. Erchiqui, Numerical investigation of a vibrationacoustic analysis with different formulations, Computer modelling in Engineering and sciences, 85 (2012) 329-345.

Highlights:

- High-frequency impact vibration and noise up to 10 kHz are successfully reproduced.
- The model is validated by a comprehensive hammer test and a pass-by measurement.
- The f_2 and pinned-pined resonances strongly influence impact vibration and noise.
- Impact vibration and track decay rate determine the main frequency of impact noise.
- This paper may contribute to the mitigation of impact vibration and noise at IRJs.